Journal of Materials Chemistry A

ROYAL SOCIETY OF CHEMISTRY

PAPER

View Article Online
View Journal | View Issue

Cite this: J. Mater. Chem. A, 2026, 14, 10633

Defect-tailored ZnO nanoflowers enable efficient, metal-free ammonia synthesis through coupled piezoelectric and photocatalytic activation

Jyh-Xuan Wang,†[a] Hsun-Yen Lin,†[a] Kuang Yuan Tu[a] and Jyh-Ming Wu *[ab]

As a sustainable and promising alternative, the nitrogen reduction reaction (NRR) has attracted growing attention for environmentally friendly ammonia production. This study presents an innovative strategy employing ZnO nanoflowers (NFs) as a catalyst for the NRR, activated through a piezo–photocatalytic mechanism. This approach enables energy harvesting from mechanical stimuli in natural environments. The intentional introduction of oxygen vacancies contributes to the generation of additional trapping centers and active sites, thereby prolonging carrier lifetime and further boosting NRR performance. Time-resolved photoluminescence (TrPL) spectroscopy reveals that ZnO samples annealed at 300 °C (denoted as ZnO-300) exhibit an extended carrier lifetime of 6 ns—three-fold higher than that of pristine ZnO. The NRR activity of ZnO-300 under the synergistic action of piezo- and photocatalysis reaches 1765.3 μg g_{cat}^{-1} h^{-1}, corresponding to a 220% increase relative to the pristine material. Complementary density functional theory (DFT) calculations corroborate the experimental findings by demonstrating that oxygen vacancies facilitate nitrogen adsorption and effectively lower the reaction energy barrier. These results underscore the potential of piezo–photocatalytic ZnO with optimized defect structures as a high-performance, metal-free catalyst for nitrogen fixation. The capability to simultaneously harvest mechanical and solar energy makes this system particularly appealing for sustainable ammonia synthesis.

Received 30th September 2025
Accepted 3rd January 2026

DOI: 10.1039/d5ta08002a

rsc.li/materials-a

1. Introduction

Ammonia (NH_3) plays a pivotal role in this context, serving not only as the primary nitrogen source for fertilizer production but also as a vital precursor in the synthesis of pharmaceuticals, refrigerants, plastics, and explosives.[1] In addition to its industrial significance, ammonia has emerged as a carbon-free fuel with high energy density, offering considerable potential for clean energy generation and contributing to the mitigation of the current global energy crisis.[2,3] The industrial Haber–Bosch process (HBP), developed over a century ago, relies on nitrogen (N_2) and hydrogen (H_2) as reactants and iron-based catalysts to produce NH_3 under high temperature (350–550 °C) and pressure (150–350 atm) conditions.[4] As a sustainable alternative to the Haber–Bosch process, the nitrogen reduction reaction (NRR) under ambient conditions has gained considerable attention.[5] Photocatalysis[6] and electrocatalysis[7] offer promising routes, yet the activation of inert N_2 molecules—due to their strong triple bond and non-polarity[8–10]—remains a major challenge. Photocatalytic NRR, in particular, utilizes sunlight to convert nitrogen and water into ammonia,[11] producing no harmful byproducts. However, practical use of the photocatalytic NRR is limited by weak light penetration, unstable solar input, and fast recombination of charge carriers.[12] To overcome these issues, methods such as defect engineering,[13] single atom doping,[14] and the formation of heterostructures[15] have been applied to enhance light absorption and charge separation.

Piezoelectric materials have inherent properties that enable them to initiate catalytic reactions even in the absence of light, thereby extending the boundaries of conventional photocatalysis.[16–18] When combined with light-driven catalysis, the piezoelectric field further enhances charge carrier separation and accelerates interfacial charge transport, resulting in superior catalytic performance.[19] Recent advances in two-dimensional transition metal dichalcogenides (2D-TMDs)—such as MoS_2,[20–22] $MoSe_2$,[23] and WS_2 (ref. 24)—have demonstrated promising piezocatalytic activity due to their excellent stability, flexibility, and tunable electronic properties.[25–31] Performance improvements have also been achieved through defect engineering,[32–34] noble metal doping,[35–37] high entropy compounds,[38] and the creation of heterostructures.[12,39] Meanwhile, traditional photocatalysts, such as TiO_2 (ref. 40) and ZnO,[41] remain attractive due to their abundance, stability, and strong oxidative ability under UV light.[42,43] In particular, ZnO, with its non-centrosymmetric wurtzite structure, exhibits

[a]Department of Materials Science and Engineering, National Tsing Hua University, 101, Section 2, Kuang-Fu Road, Hsinchu 300, Taiwan. E-mail: wujm@mx.nthu.edu.tw
[b]High Entropy Materials Center, National Tsing Hua University, 101, Section 2, Kuang-Fu Road, Hsinchu 300, Taiwan
† These authors contributed equally.

intrinsic piezoelectricity,[44] making it a uniquely suitable platform for hybrid piezo–photocatalytic systems. Despite these advancements, the synergistic integration of piezoelectricity and photocatalysis for the nitrogen reduction reaction remains largely underdeveloped, especially using simple and scalable material architectures.

To address this challenge, piezo–photocatalysis[45–47] has emerged as a transformative strategy. By coupling mechanical and solar energy inputs, this approach generates enhanced internal electric fields that promote directional charge separation and facilitate multi-electron transfer reactions critical for the NRR. This dual activation strategy opens up a new pathway for efficient, bias-free ammonia synthesis, particularly under low-energy and decentralized conditions. Our work introduces a novel and rationally designed ZnO nanoflower (NF) catalyst with controlled oxygen vacancies as a structurally simple yet highly effective piezo–photocatalyst for the NRR.[48,49] Unlike prior systems that rely on complex heterostructures or noble metal additives, our design leverages intrinsic material properties—optimized through defect engineering—to simultaneously boost piezoelectric and photocatalytic activity.[32] Both experimental results and DFT simulations reveal that a moderate concentration of oxygen vacancies not only enhances nitrogen adsorption but also lowers the energy barrier of the reaction, resulting in a remarkable ammonia yield. To our knowledge, this is among the highest reported performances for a metal-free, mono-component ZnO system. As illustrated in Fig. 1a, we propose a ZnO–O_V-assisted NRR pathway in which end-on N_2 is stepwise hydrogenated through key N_x–H_y intermediates. This design integrates simplicity, scalability, and multifunctionality—providing a practical route to sustainable NH_3 production *via* ambient-energy harvesting and defect-engineered nanomaterials.

2. Results and discussion

To clarify how oxygen vacancies (O_V) promote nitrogen activation, DFT calculations were performed, as corroborated by the results described below. Fig. 1a and b proposed a piezocatalytic hydrogenation pathway on ZnO containing oxygen vacancies (O_V). Molecular N_2 adsorbs end-on at O_V sites, where ultrasonically induced piezoelectric polarization drives interfacial electron injection into the N_2 π^* antibonding orbital, weakening and elongating the N–N bond. Successive proton/electron transfers yield *NNH → *NHNH → *NH_2NH_2, followed by N–N cleavage to *NH_x fragments that are further hydrogenated to NH_3. Periodic polarization reversals promote charge separation at the vacancy–ZnO interface and sustain the reduction steps, after which NH_3 desorbs and the active O_V site is regenerated.

Based on these insights, we synthesized ZnO NFs and introduced different levels of oxygen vacancies by annealing at various temperatures. This approach allows us to explore the relationship between structural changes and nitrogen reduction performance. By linking theory with experiments, we aim to clarify the role of oxygen vacancies in improving piezo–photocatalytic activity. Fig. 1c and d present the field-emission scanning electron microscopy (FE-SEM) images of the ZnO-300 sample (annealing at 300 °C), revealing a uniform nanoflower architecture with an average diameter of ~1 μm. The inset shows a single well-defined nanostructure, confirming the successful formation of flower-like morphologies. Comparative SEM analysis (Fig. S1, SI) demonstrates that this nanoflower structure is preserved across annealing treatments, indicating high structural robustness and thermal stability. X-ray diffraction (XRD) patterns (Fig. 1e) of ZnO NFs annealed at different temperatures exhibit sharp diffraction peaks corresponding to the wurtzite ZnO phase (JCPDS no. 79-0206),[50] with enhanced peak intensity observed upon annealing at 300 °C. However, further increases in annealing temperature (400–500 °C) lead to a decline in crystallinity, likely due to excessive defect formation and lattice disorder. Transmission electron microscopy (TEM) further corroborates these observations. As shown in Fig. 1f, the ZnO-300 NFs consist of densely packed petal-like structures, confirming the spherical flower morphology. High-resolution TEM imaging of the edge region (Fig. 1g and h) reveals well-aligned crystalline domains. The HRTEM image in Fig. 1i displays clear lattice fringes with an interplanar spacing of 0.248 nm, corresponding to the (101) plane of ZnO.[51–53] The accompanying fast Fourier transform (FFT) and selected area electron diffraction (SAED) patterns confirm the presence of the (101) and (002) planes (inset in Fig. 1i), in agreement with XRD analysis. To probe the evolution of oxygen defect states, X-ray photoelectron spectroscopy (XPS) was performed. The chemical composition and defect states of ZnO NFs were investigated by X-ray photoelectron spectroscopy (XPS). Fig. S2 (SI) present the high-resolution O 1s spectra of ZnO samples annealed at varying temperatures (pristine, 300 °C, 400 °C, and 500 °C). Each spectrum can be deconvoluted into three peaks centered at ~530.0 eV, 531.4 eV, and 532.4 eV, attributed to lattice oxygen (O_L), oxygen vacancies (O_V), and surface chemisorbed oxygen species (O_C), respectively.[54] Quantitative analysis indicates that the oxygen vacancy content increases from 18% in pristine ZnO to 29% in ZnO-500 (Fig. 1j), confirming that thermal annealing in a reducing atmosphere effectively modulates the defect concentration. The O_C species are likely associated with surface hydroxyl groups and adsorbed water from the hydrothermal synthesis process. Fig. 1k displays the Zn 2p spectra, with binding energies of 1020.7 eV and 1043.8 eV corresponding to Zn $2p_{3/2}$ and Zn $2p_{1/2}$, respectively, consistent with Zn^{2+} oxidation states.[52] A progressive shift to higher binding energies is observed with increasing annealing temperature, which can be attributed to the increased electron localization induced by oxygen vacancies. This shift reflects an enhanced local positive potential near the Zn nucleus due to the reduced screening of core electrons, providing further spectroscopic evidence of defect formation.

Electron paramagnetic resonance (EPR) spectroscopy (Fig. 2a) identifies a characteristic peak at a *g*-factor of ~2.004, indicative of oxygen vacancy defects.[49] The increasing intensity of EPR signals with rising annealing temperatures confirms that the concentration of oxygen vacancies in ZnO NFs can be effectively modulated through thermal treatment. Higher annealing temperatures result in a greater density of oxygen

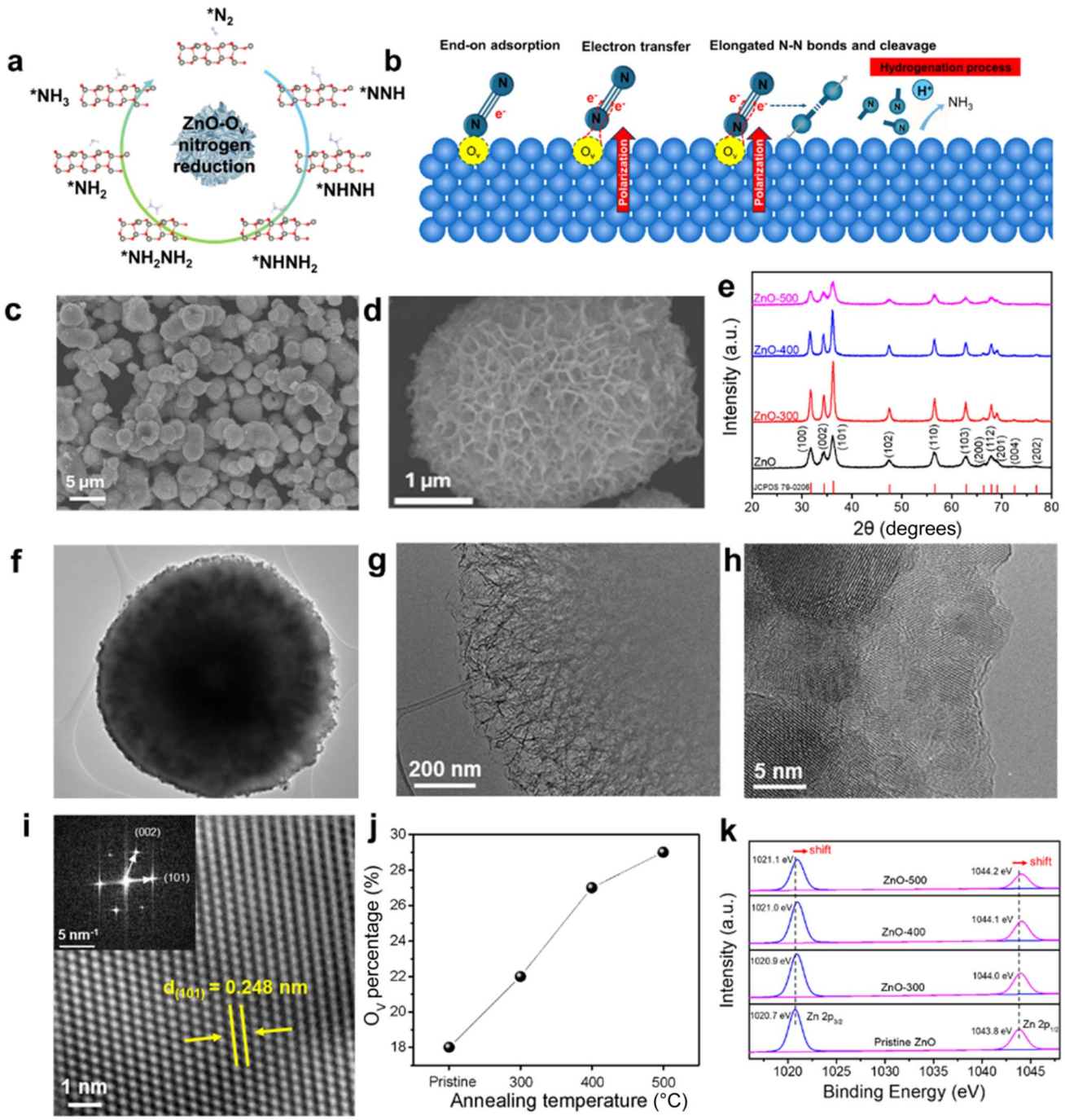

Fig. 1 (a) Schematic of the proposed ZnO–O_V-assisted nitrogen-reduction pathway showing key N_xH_y species intermediates. (b) Schematic of the piezocatalytic hydrogenation pathway on ZnO with oxygen-vacancy sites (O_V). N_2 adsorbs end-on at O_V, piezoelectric polarization drives electron injection into the π* orbitals to weaken the elongated N–N bond, followed by stepwise H addition and N–N cleavage to form NH_3. (c) Low-magnification FE-SEM of ZnO-300 nanoflowers (scale: 5 μm). (d) SEM of a single ~1 μm nanoflower (scale: 1 μm). (e) XRD patterns of nanoflowers annealed at different temperatures, confirming hexagonal wurtzite ZnO. (f) Low-magnification TEM of a ZnO-300 nanoflower. (g) Edge-resolved TEM showing petal-like nanosheets radiating from the core (scale: 200 nm). (h) HRTEM revealing clear lattice fringes across the petals (scale: 5 nm). (i) Atomic-resolution HRTEM of ZnO-300 with $d_{(101)} = 0.248$ nm; inset: SAED/FFT indexed to the (101) and (002) planes (scale: 5 nm^{-1}). (j) Oxygen-vacancy (O_V) percentage extracted from O 1s deconvolution *vs.* annealing temperature. (k) XPS Zn 2p spectra at different annealing temperatures showing a gradual positive binding-energy shift, indicative of increasing O_V concentration.

vacancies, indicating a direct correlation between thermal activation and defect formation. Fig. 2b presents the photoluminescence (PL) spectra of both pristine and annealed ZnO NFs. All spectra exhibit two characteristic emission peaks: one at approximately 380 nm, corresponding to near-band-edge (NBE) emission, and another around 515 nm, associated with deep-level emission (DLE). The DLE peak is primarily attributed to the radiative recombination of charge carriers involving

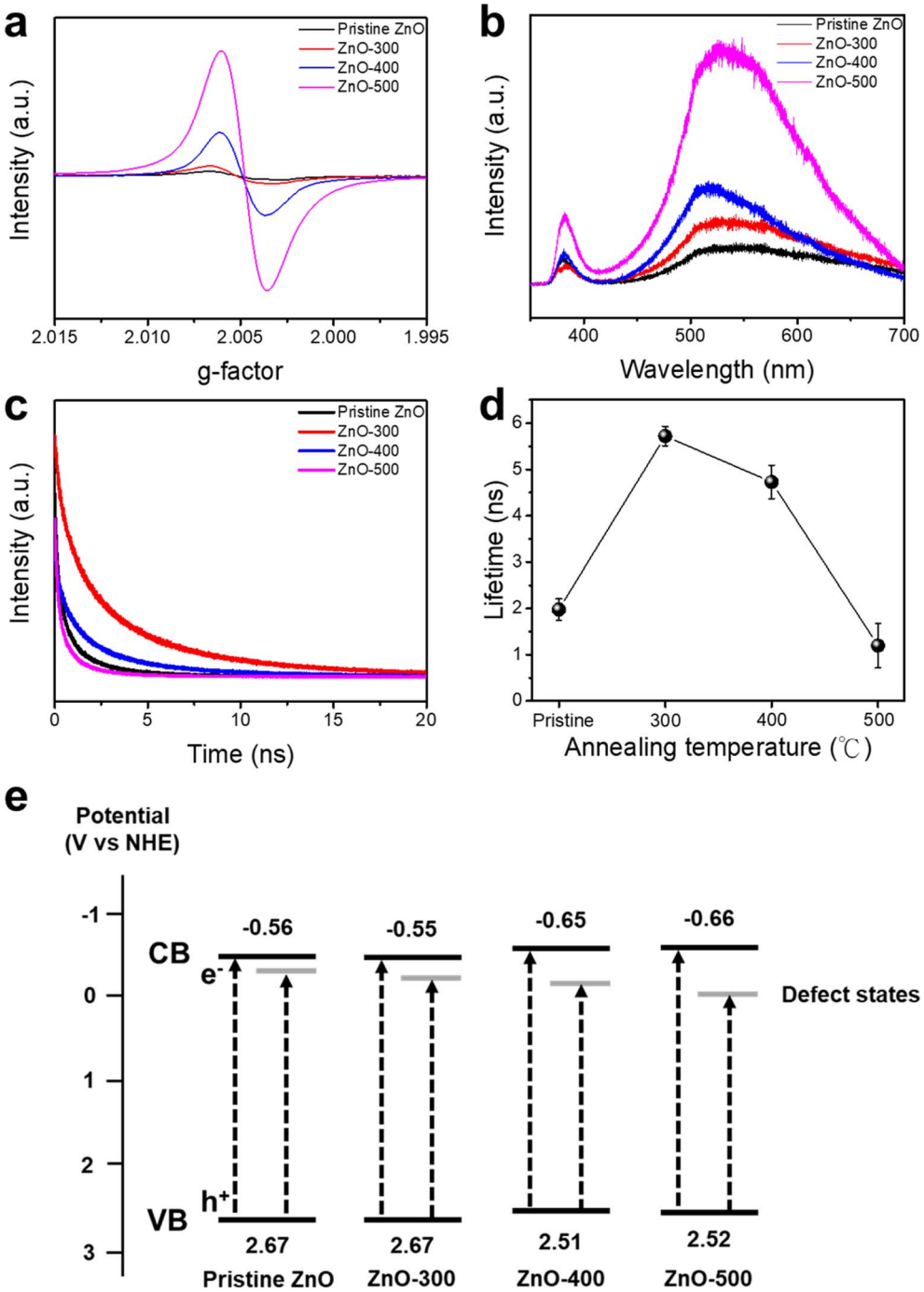

Fig. 2 (a) EPR spectra of ZnO nanoflowers annealed at different temperatures, showing the evolution of unpaired electron density related to oxygen vacancies. (b) Photoluminescence (PL) spectra of ZnO nanoflowers, highlighting defect-related emission intensity changes with varying annealing temperatures. (c) Time-resolved photoluminescence (TrPL) decay spectra of ZnO nanoflowers, used to evaluate charge carrier recombination behavior. (d) Carrier lifetimes extracted from biexponential fitting of TrPL decay curves in (c), demonstrating prolonged lifetimes for samples with higher oxygen vacancy concentrations. (e) Schematic band structure of ZnO samples, illustrating the formation of deeper defect states associated with increased oxygen vacancy levels induced by thermal treatment.

defect states, particularly oxygen vacancies acting as electron trapping centers.[32] The increasing PL intensity with higher annealing temperatures suggests a progressive rise in oxygen defect concentrations, which facilitates the formation of more trapping centers on the ZnO surface.[54] The emission peak at ~515 nm corresponds to an energy level of ~2.4 eV and is indicative of defect states introduced by oxygen vacancies. Time-resolved photoluminescence (TrPL) measurements were employed to evaluate the carrier lifetimes of photoexcited electron–hole pairs (Fig. 2c and d). The results reveal that the ZnO-300 sample exhibits the longest carrier lifetime among all samples, indicating a reduced recombination rate attributed to

a moderate concentration of oxygen vacancies. These vacancies serve as shallow trapping centers, thereby prolonging the lifetime of charge carriers by suppressing recombination within the bandgap. However, further increases in annealing temperature to 400 °C and 500 °C lead to a noticeable decrease in carrier lifetime. This reduction is attributed to the excessive generation of oxygen vacancies, which introduce deeper defect states below the conduction band. Such deep-level defects not only trap electrons but also facilitate the recombination of holes, thereby increasing the overall recombination rate. These findings suggest that while moderate oxygen vacancy concentrations enhance charge separation, excessive defect densities can act as recombination centers, ultimately diminishing photocatalytic efficiency.[32,55] Fig. 3e presents a schematic energy

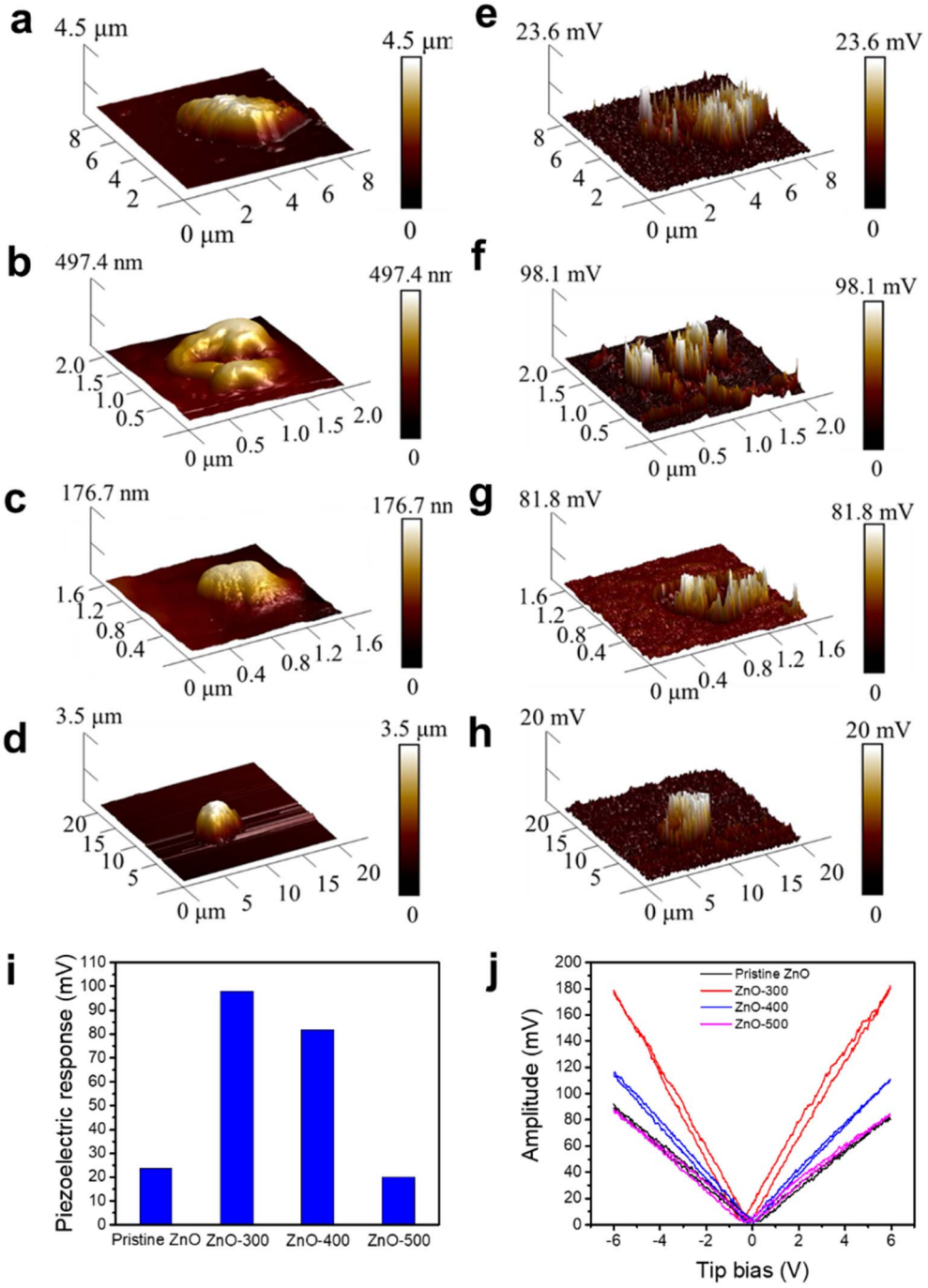

Fig. 3 (a–d) AFM topography images of pristine ZnO, ZnO-300, ZnO-400, and ZnO-500, respectively. (e–h) Corresponding PFM amplitude images showing the piezoresponse of pristine ZnO, ZnO-300, ZnO-400, and ZnO-500, respectively. (i) Quantitative comparison of the piezoresponse amplitudes among all samples. (j) Butterfly loops of ZnO nanoflowers annealed at different temperatures, illustrating the evolution of piezoelectric behavior.

band diagram constructed based on the optical band gaps determined from UV-vis diffuse reflectance spectroscopy (UV-DRS, Fig. S3, SI of S1) and valence band maximum (VBM) values obtained from XPS analysis (Fig. S4, SI of S2). The results reveal a gradual narrowing of the band gap—from 3.29 eV (for pristine ZnO) to 3.16 eV (for ZnO-500)—accompanied by a downward shift in the VBM from 2.67 eV to 2.52 eV with increasing annealing temperature. These changes are indicative of increasing oxygen vacancy concentration, which introduces mid-gap defect states and modifies the electronic structure. The diagram also includes the estimated positions of these defect levels, inferred from PL spectra, showing their deepening and density enhancement as the annealing temperature rises.

The piezoelectric properties of pristine and annealed ZnO NFs were systematically investigated using piezoresponse force microscopy (PFM). Fig. 3a–d present the atomic force microscopy (AFM) topography images of pristine ZnO, ZnO-300, ZnO-400, and ZnO-500, respectively, while Fig. 3e–h show their corresponding piezoresponse amplitude images. A comparative analysis reveals a substantial enhancement in the piezoelectric response for the ZnO-300 sample, which exhibits a piezoelectric output voltage of 98.1 mV, significantly higher than the 23.6 mV recorded for pristine ZnO. The quantitative comparison of piezoelectric responses is summarized in Fig. 3i. The progressive increase in piezoresponse from pristine ZnO to ZnO-300 is attributed to two key factors: the formation of local non-centrosymmetric structures in the vicinity of oxygen vacancies, and improved crystallinity induced by moderate annealing. Both effects contribute to enhanced polarization and, consequently, a stronger piezoelectric effect.[32,56] However, further

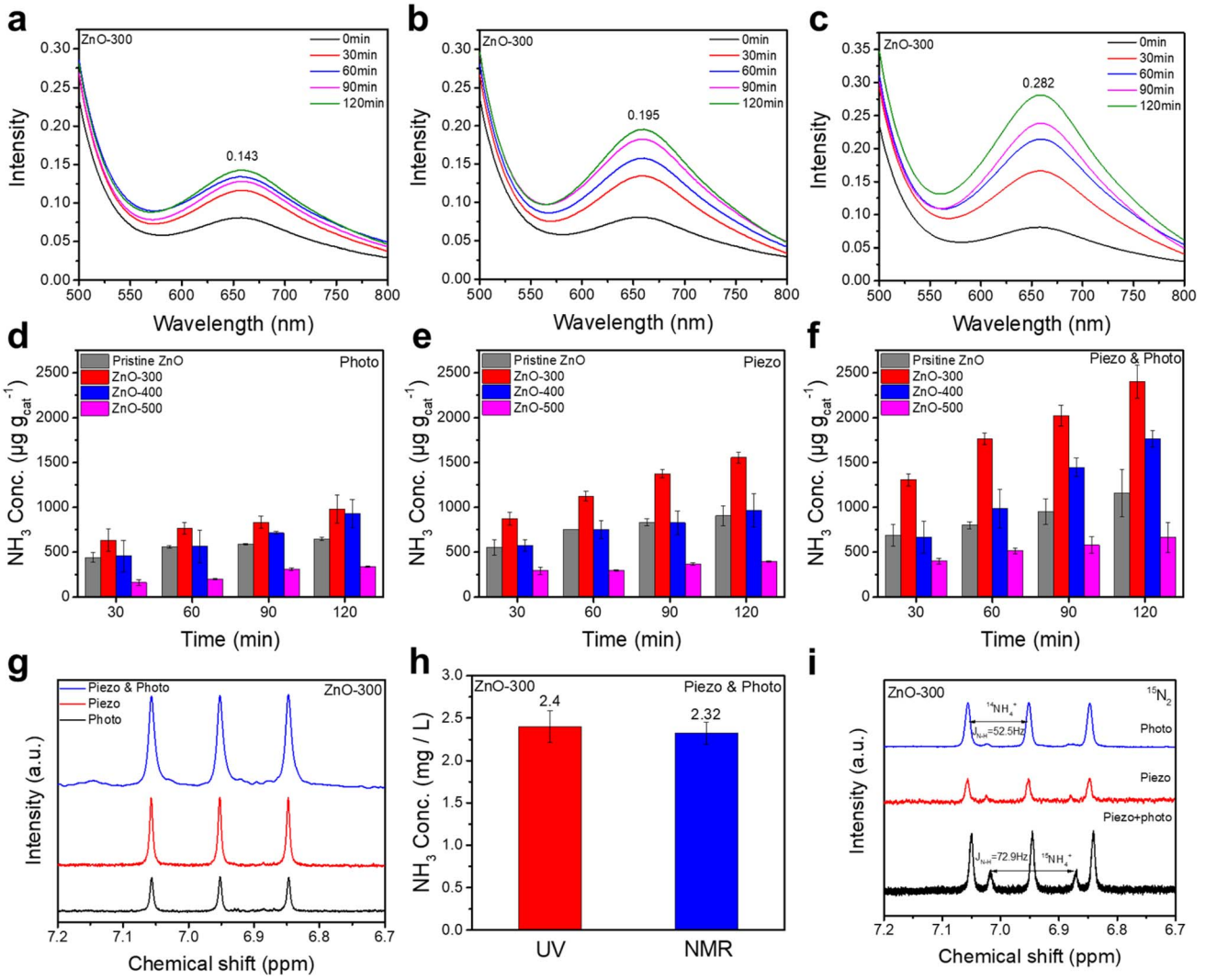

Fig. 4 Time-dependent UV-vis spectra of ZnO-300 by (a) light irradiation only (photo), (b) ultrasonic vibration only (piezo), and (c) coupling ultrasonic vibration and light irradiation (piezo & photo). NRR performance of ZnO NFs under different annealing temperatures by (d) photo, (e) piezo, and (f) piezo & photocatalytic processes. (g) ^{1}H NMR spectra of ZnO-300 after treatment under different experimental conditions, confirming ammonia generation. (h) Comparison of NH_3 concentration from ZnO-300 under piezo–photocatalytic conditions, quantified by various analytical methods. (i) ^{1}H NMR spectra showing the distinction between $^{15}NH_4^+$ and $^{14}NH_4^+$, verifying nitrogen source incorporation during piezo–photocatalytic reactions for ZnO-300.

increases in annealing temperature to 400 °C and 500 °C result in a decline in piezoelectric performance. This reduction is likely due to structural degradation caused by an excessive concentration of oxygen vacancies, which disrupts the long-range crystal order, as corroborated by XRD analysis. Such degradation leads to diminished crystallinity and a corresponding reduction in piezoelectric characteristics.[57–59] Fig. 3j illustrates the PFM amplitude–voltage (butterfly) loops for samples annealed at different temperatures. All samples exhibit the characteristic butterfly-shaped curves indicative of piezoelectric behavior. Notably, the ZnO-300 sample displays the highest amplitude response, further confirming its superior piezoelectric performance relative to other samples.

2.1 NRR performance

The nitrogen reduction reaction (NRR) experiments were conducted under three distinct catalytic conditions: photocatalysis, piezocatalysis, and combined piezo–photocatalysis, all performed without the addition of any sacrificial agent. The corresponding UV-visible absorption spectra for the ZnO-300 sample under each condition over a 120 minute reaction period are shown in Fig. 4a–c. Ammonia production was quantified by converting absorption intensity values into ammonia yield using a pre-established calibration curve (Fig. S5a and b). Fig. 4d–f present the corresponding ammonia yield of ZnO NFs annealed at different annealing temperatures, evaluated under each set of catalytic conditions. Among all samples, ZnO-300 exhibited the highest catalytic activity across photocatalytic, piezocatalytic, and piezo–photocatalytic processes. This performance trend aligns with the findings from TrPL and PFM analyses, underscoring the importance of charge carrier lifetime and piezoelectric properties in enhancing catalytic performance. Specifically, the optimal ammonia yield rates for ZnO-300 after 1 hour of reaction were 767.9, 1124.1, and 1765.3 $\mu g\ g_{cat}^{-1}\ h^{-1}$ under photocatalytic, piezocatalytic, and piezo–photocatalytic conditions, respectively—representing enhancements of 138%, 150%, and 220% over pristine ZnO. To ensure the reliability of the observed results and exclude potential artifacts, two control experiments were performed: one in the absence of nitrogen and the other without catalytic activity. The primary byproduct of the NRR, hydrazine (N_2H_4), was analyzed using the Watt and Chrisp method, with the calibration data provided in Fig. S6a and b (SI). As shown in Fig. S7a (SI), the control experiments were designed to confirm the essential role of each component—N_2 gas, ultrasonication (U), and light irradiation (L)—in the piezo–photocatalytic nitrogen reduction reaction. The N_2 + U + L condition represents the complete catalytic system, where ZnO-300 was exposed simultaneously to nitrogen gas, ultrasonication, and light irradiation. This setup shows a significant absorption peak, indicating successful ammonia production. In contrast, the N_2-only condition (with nitrogen gas flow but without ultrasonication or light) shows negligible ammonia formation, confirming that the catalyst remains inactive in the absence of energy input. Similarly, the U + L condition (with ultrasonication and light but no nitrogen gas) also shows no ammonia signal, highlighting the necessity of molecular nitrogen as the reactant. These results strongly demonstrate that only the combined presence of nitrogen gas and dual energy inputs—mechanical (ultrasound) and photonic (light)—can activate ZnO-300 for efficient ammonia synthesis, reinforcing the synergistic nature of the piezo–photocatalytic process. Fig. S7b further shows that no detectable hydrazine was produced under any reaction conditions, demonstrating the high selectivity of the ZnO-300 catalyst toward ammonia formation. To further validate the ammonia production, quantitative analysis was performed using proton nuclear magnetic resonance (^{1}H NMR) spectroscopy.

Ammonium ion concentrations ($^{14}NH_4^+$) were determined by integrating the characteristic peak areas and converting them to ammonia yields *via* a separate calibration curve (Fig. S8a and b). The concentrations of ammonia detected by NMR were 0.77, 1.40, and 2.32 mg l^{-1} for photocatalytic, piezocatalytic, and piezo–photocatalytic processes, respectively. These values closely match the results obtained *via* the indophenol blue method, as shown in the comparative analysis in Fig. 5h. To further investigate the reaction mechanism, isotope-labeled nitrogen experiments were conducted using nitrogen-15 gas ($^{15}N_2$) gas as the nitrogen source. In this test, 10 ml of $^{15}N_2$ was introduced into deionized water prior to the catalytic reaction. The ^{1}H NMR spectra of ZnO-300 under piezo–photocatalytic conditions (Fig. 4i) reveal two characteristic coupling constants at 52.5 Hz and 72.9 Hz, corresponding to $^{14}NH_4^+$ and $^{15}NH_4^+$, respectively.[60] While the natural abundance of $^{15}N_2$ is only 0.4%, a markedly enhanced $^{15}NH_4^+$ signal was observed under piezo–photocatalysis, confirming the successful reduction of isotopically labeled $^{15}N_2$. The NMR results of the photocatalytic and piezocatalytic processes are shown in Fig. S9a and b. Notably, the distinct 72.9 Hz doublet is significantly stronger than that under the individual photo or piezo conditions, highlighting the synergistic enhancement of the combined process. These isotope-labeling results provide robust evidence that the ammonia originates from the introduced $^{15}N_2$, ruling out contamination and affirming the intrinsic catalytic activity of ZnO-300. This validation underscores the catalyst's selectivity and its potential as a sustainable, metal-free platform for ambient nitrogen fixation *via* coupled mechanical and photonic energy input. A comparative summary of ammonia production rates across various catalytic systems and materials is presented in Table S1, further validating the high NRR activity and selectivity of the ZnO-300 catalyst.[61]

2.2 DFT simulations and mechanism

To further elucidate the experimental findings and understand the underlying reaction mechanisms, density functional theory (DFT) simulations were performed (SI of S3). Two surface models were constructed for analysis: pristine ZnO and ZnO–O_V, as illustrated in Fig. S10. For both models, nitrogen adsorption was found to be most favorable at hollow sites *via* an end-on configuration (Fig. S11). Fig. 5a presents the nitrogen adsorption energies for each model. The introduction of oxygen vacancies significantly lowers the nitrogen adsorption energy, suggesting that N_2 molecules interact more readily with the

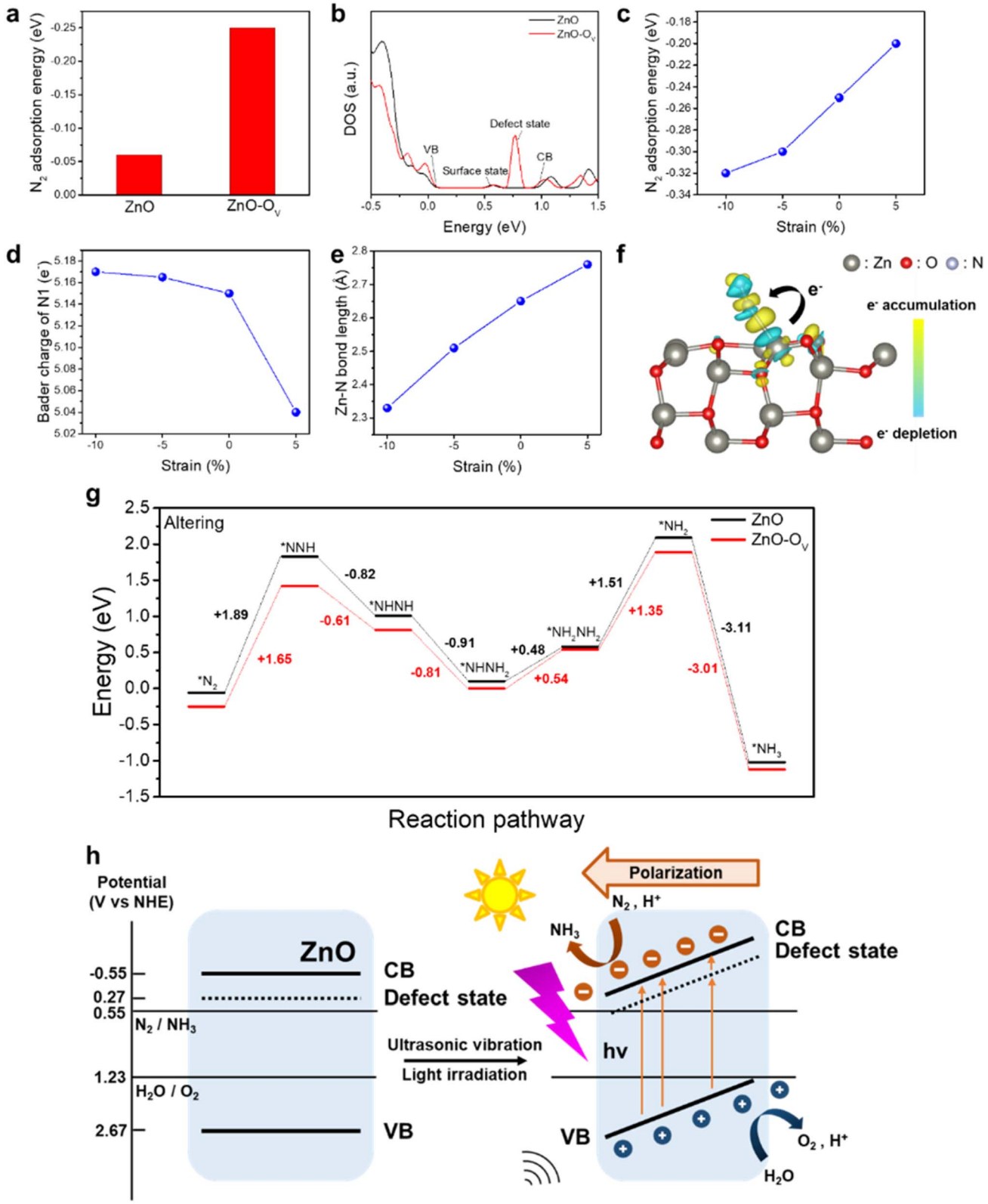

Fig. 5 (a) Nitrogen adsorption energies on the surfaces of pristine ZnO and oxygen-deficient ZnO (ZnO–O_V), obtained *via* DFT calculations. (b) Density of states (DOS) of ZnO and ZnO–O_V, showing defect-induced mid-gap states in ZnO–O_V. (c–e) Effects of applied mechanical strain on the ZnO–O_V surface after nitrogen adsorption: (c) nitrogen adsorption energy, (d) Bader charge of adsorbed nitrogen, and (e) Zn–N bond length. (f) Charge density difference (CDD) map of ZnO–O_V under 10% compressive strain, highlighting electron accumulation and depletion regions. (g) Free energy diagram of the nitrogen reduction reaction (NRR) on ZnO and ZnO–O_V *via* the associative alternating pathway. (h) Schematic diagram illustrating the energy band structure of ZnO with oxygen vacancies (left), and the proposed working mechanism under simultaneous light irradiation and ultrasonic vibration (right). The piezoelectric polarization field facilitates charge separation and directional migration, promoting enhanced NRR activity on ZnO–O_V.

$ZnO–O_V$ surface than with pristine ZnO. To gain further insight into the electronic interactions during adsorption, Bader charge analysis was conducted.[62–65] Focusing on the nitrogen atom closest to the surface (denoted as N1), which is most likely to engage in charge transfer, the initial atomic charge of 4.97 increased to 4.99 for pristine ZnO and to 5.15 for $ZnO–O_V$ after adsorption. These results confirm that nitrogen atoms are reduced upon adsorption and that oxygen vacancies facilitate a greater degree of electron transfer, thereby enhancing the reduction potential of the adsorbed N_2 molecule. The density of states (DOS) profiles for both pristine ZnO and $ZnO–O_V$ are shown in Fig. 5b, with the energy axis aligned at 0 eV relative to the valence band maximum (VBM). Both models exhibit surface states, likely due to the surface nature of the slab model. Notably, the $ZnO–O_V$ model exhibits an additional gap state at ~0.75 eV near the conduction band, which can be attributed to the defect level introduced by the oxygen vacancy. Although the bandgap predicted by DFT underestimates the experimental value, this limitation is a well-known artifact of conventional DFT calculations.[66] To simulate the condition of ultrasonic vibration applied on piezocatalyst materials, different percentages of strain were applied to the $ZnO–O_V$ model for further investigation. Fig. 5c–e shows the results of N_2 adsorption energy, Bader charge of the N1 site, and Zn–N bond length of $ZnO–O_V$ under different percentages of applied strain, respectively. The results indicate that under 10% of compressive strain, the lowest adsorption energy, the highest Bader charge, and the shortest Zn–N bond length can be obtained.[67,68] We note that similar strain amplitudes have been widely used in theoretical studies of piezoelectric semiconductors to model ultrasonic or mechanical-field-induced piezopotentials, further supporting the validity of the 10% strain approximation.[68,69] The results indicate that with the assistance of applied strain, the nitrogen atoms may become easier to be adsorbed onto the surface of the catalyst and charge transfer can be facilitated. Moreover, the Zn–N bond length can be correlated with the Zn–N bond strength, namely the shorter the bond length, the higher the bond strength. Fig. 5f displays the charge density difference (CCD) image of $ZnO–O_V$ with 10% of compressive strain. The result demonstrates that the electron has been transferred from the catalyst's surface to nitrogen. Also, the electron transfer from one nitrogen atom to the other may lead to the weakening of the nitrogen bond, allowing the nitrogen molecule to dissociate more easily. In the catalytic NRR, the associative pathway is the most common reaction pathway. It can be further divided into altering and distal mechanisms by different hydrogenation sequences.[70] The nitrogen molecule will first adsorb on the catalyst's surface and then undergo a series of hydrogenation processes, including the multiple $H^+–e^-$ transfer processes, and the final product will be NH_3. Fig. 5g shows the NRR free energy diagram of ZnO and $ZnO–O_V$ through the associative altering reaction pathway, which is the most energy-favorable pathway in our catalytic system. The result shows that the potential determining step on both ZnO and $ZnO–O_V$ is the first hydrogenation process ($*N_2 \rightarrow *NNH$),[71,72] with the reaction energy barriers of 1.89 and 1.65 eV, respectively. It is noteworthy that the energy barrier of $ZnO–O_V$ is lower than that of ZnO, which also proves that the existence of oxygen vacancy can lower the energy barrier of the NRR. The free energy diagrams of associative distal and mixed pathways are shown in Fig. S12a and b, respectively. These additional free energy diagrams reveal that both the associative distal and mixed pathways exhibit higher overall energy barriers compared to the associative alternating pathway, making them less favorable under the current catalytic system. Specifically, the distal pathway involves a more energetically demanding sequence of hydrogenation steps, while the mixed pathway, although somewhat improved, still presents a higher energy hurdle relative to the alternating route. Therefore, the associative alternating pathway remains the most thermodynamically viable mechanism for the NRR over both ZnO and $ZnO–O_V$ surfaces. Furthermore, the step-by-step transformation schematic illustrated in Fig. 1a as mention provides a clear visual representation of the hydrogenation sequence on $ZnO–O_V$, highlighting the role of surface-bound intermediates and electron transfer during the NRR. Taken together, these results confirm that oxygen vacancies not only enhance N_2 adsorption and charge transfer but also shift the reaction pathway toward the most energetically favorable route, thereby optimizing the overall catalytic efficiency of $ZnO–O_V$ for ammonia production.

In addition to the static adsorption and reaction-energy analyses above, it is important to note that the synergistic enhancement observed experimentally can also be interpreted through the lens of strain–defect coupling and field-assisted charge migration. The introduction of oxygen vacancies not only strengthens N_2 chemisorption but also locally distorts the lattice, creating regions with enhanced polarizability. Under mechanical agitation, these defect-rich domains respond more strongly to applied strain, leading to localized polarization amplification. Such strain–defect coupling effects promote additional electron density redistribution toward adsorbed N_2, consistent with our computed charge-density-difference maps. Moreover, the piezoelectric polarization generated under ultrasonic excitation can be viewed as establishing a polarization-potential landscape across the $ZnO–O_V$ surface. This internal field is expected to lower migration barriers for surface electrons, facilitating field-assisted charge transport toward the N_2 reduction sites. Although explicit polarization-potential modeling or nonadiabatic charge-migration simulations are beyond the scope of the present study, the experimental trends—enhanced carrier separation, prolonged lifetime, and superior NRR performance under coupled excitation—are fully consistent with such field-assisted mechanisms.

Fig. 5h illustrates the proposed working mechanism of piezo–photocatalytic NRR over ZnO with oxygen vacancies, including the associated potentials for nitrogen reduction and water oxidation.[11] The energy band structure, derived from UV-vis diffuse reflectance spectroscopy and XPS-VBM (Fig. S3 and S4), supports the mechanistic framework. Upon light excitation, electrons are excited from the valence band (VB) to the conduction band (CB), as represented by eqn (1), leaving behind photogenerated holes in the VB. Electron transitions can also occur from mid-gap defect states introduced by oxygen vacancies to the CB. Simultaneously, strain-induced piezoelectric

polarization generates an internal electric field that drives spatial separation of charge carriers, enhancing the suppression of recombination.[32] The holes will then participate in the water oxidation reaction to oxidize H_2O into O_2, as represented in eqn (2). In the meantime, electrons and the released H^+ will participate in the N_2 reduction reaction to form NH_3 through multiple H^+–e^- transfer processes and the hydrogenation sequences shown in the DFT simulations,[11] as shown in eqn (3) and SI S4. The total NRR can be expressed as eqn (4). The combination of oxygen vacancy engineering and mechanical strain synergistically enhances photocatalytic performance. Oxygen vacancies extend carrier lifetimes by acting as shallow traps, while piezoelectric polarization promotes directional charge separation. Together, these effects enable highly efficient and selective nitrogen fixation under piezo–photocatalytic conditions.

$$ZnO \xrightarrow{\text{excitation}} h^+ + e^- \quad (1)$$

$$H_2O \rightarrow \frac{1}{2}O_2 + 2H^+ + 2e^- \quad (2)$$

$$N_2 + 6H^+ + 6e^- \rightarrow 2NH_3 \quad (3)$$

$$2N_2 + 6H_2O \rightarrow 4NH_3 + 3O_2 \quad (4)$$

3. Conclusions

This study establishes a significant breakthrough in sustainable ammonia synthesis by demonstrating that structurally simple ZnO nanoflowers (NFs), when engineered with controlled oxygen vacancies (ZnO–O_V), can serve as highly efficient and metal-free catalysts under ambient conditions. By harnessing the synergistic effects of photocatalysis and piezoelectricity, the system achieves superior nitrogen reduction activity without the need for external bias or sacrificial agents. The incorporation of a moderate concentration of oxygen vacancies plays a pivotal dual role: it introduces defect levels that act as shallow traps to significantly prolong the lifetime of photogenerated carriers, and it creates highly active adsorption sites that drastically improve the affinity for N_2 molecules. These defect-induced enhancements are further amplified under mechanical strain, where the piezoelectric polarization field induces asymmetric band bending. This internal field accelerates spatial charge separation, reduces recombination losses, and promotes directional charge transfer to surface-active sites. TrPL measurements confirmed the prolonged carrier lifetime in ZnO–O_V, while DFT calculations demonstrated a notable reduction in nitrogen adsorption energy and reaction barriers compared to pristine ZnO. The reaction pathway analysis also reveals that ZnO–O_V favors the associative alternating mechanism with a lower energy barrier, further validating the intrinsic catalytic advantage introduced by oxygen vacancies. Remarkably, under piezo–photocatalytic conditions, the ZnO-300 catalyst achieved an ammonia yield of 1765.3 μg g_{cat}^{-1} in just one hour—among the highest reported for nanocomponent, metal-free catalysts. These results not only showcase the transformative effect of vacancy engineering but also highlight the feasibility of ambient-energy-driven catalysis using light and mechanical stimuli. This work paves the way for the rational design of next-generation, environmentally friendly NRR catalysts that combine structural simplicity, scalable fabrication, and exceptional performance. The integration of ZnO–O_V and piezoelectric enhancement offers a practical and compelling pathway for clean ammonia production and decentralized green energy solutions.

4. Experimental section

4.1 Preparation of pristine ZnO

In this work, ZnO NFs are synthesized by the hydrothermal method. The precursors, including $Zn(CH_3COO)_2 \cdot 2H_2O$ (99%, Showa), $C_6H_{12}N_4$ (99%, Alfa), and $Na_3C_6H_5O_7$ (99%, Thermo Scientific), are firstly dissolved in 60 ml of distilled water (DI) and magnetically stirred for twenty minutes at room temperature. After completely dissolving, the solution is transferred into a Teflon-lined stainless-steel autoclave of 100 ml capacity, followed by the hydrothermal process in an oven at 90 °C for 3 hours. After that, the sample is washed with DI water and ethanol alternatively and dried in an oven at 60 °C for 12 hours, followed by the annealing treatment under ambient air at 300 °C for 1 h to remove the residual elements on the surface of ZnO and increase the crystallinity. The product was referred to as pristine ZnO.

4.2 Synthesis of ZnO with oxygen vacancy

To create different oxygen vacancy concentrations, the pristine ZnO underwent a thermal-annealing treatment conducted in a furnace with a vacuum pump in an Ar/H_2 (5% H_2) mixed gas environment at different temperatures for 3 hours to obtain the final products, denoted as ZnO-T. For instance, ZnO-300 refers to ZnO after annealing treatment under Ar/H_2 mixed gas at 300 °C for 3 h.

4.3 Characterization analysis

A field-emission scanning electron microscope (FESEM, HITACHI, SU8010) and X-ray diffractometer (XRD Bruker D2 Phaser) were employed to investigate the morphologies and crystal structures of the as-prepared samples, respectively. Transmission electron microscopy (TEM, JEOL ARM-200F) was conducted to further investigate the crystal structures and lattice arrangement. X-ray photoelectron spectroscopy (XPS, Thermo Fisher Scientific ESCALAB Xi^+) was used to determine the surface chemical and electronic states, elemental composition, and concentration of impurities of the as-synthesized samples. Electron paramagnetic resonance (EPR, BRUKER ESR 5000), photoluminescence (PL, Horiba Jobin Yvon LABRAM HR 800 UV), and time-resolved photoluminescence (TRPL, HORIBA Jobin Yvon) were employed to analyze the defect-related properties. Piezo-response force microscopy (PFM, Bruker Dimension ICON) was applied to analyze the piezoelectric response,

height profile, and surface potential of the samples. Ammonia production through the catalytic reaction was analyzed through ultraviolet-visible spectroscopy (UV-vis, HITACHI U-3900) and nuclear magnetic resonance (NMR, JEOL NMR 500).

4.4 Catalytic reaction and ammonia quantification

In this work, we conducted the nitrogen reduction reaction experiment under three different conditions, including ultrasonication, light irradiation, and ultrasonication combined with light irradiation. Ultrasonication was simulated using an ultrasonic cleaner (Delta, DC 300, 300 W, 40 kHz). A 100 W xenon lamp was used for light irradiation. Specifically, 10 mg of ZnO powder were mixed with DI water, which was pre-pumped with nitrogen gas (99.999%) overnight. The mixture was placed in a 25 ml sample bottle without a lid, followed by the nitrogen reduction experiment under different conditions with nitrogen pumping simultaneously with a flow rate of 100 sccm. The solution was sampled for further quantification of ammonia every 30 minutes. A water bath in the ultrasonic cleaner was renewed frequently to ensure there was negligible temperature change during the catalytic process. For $^{15}N_2$ isotope analysis, $^{15}N_2$ gas (≥99.8 atom% ^{15}N, Sigma Aldrich) was used. A 25 ml freezing apparatus was filled with 10 ml of deionized water. The system was frozen with liquid nitrogen and air-extraction by a pump to eliminate gas dissolved in the water for 2 hours. The apparatus was then allowed to reach room temperature, followed by purging 25 ml of $^{15}N_2$ gas into the container. After leaving undisturbed for 2 hours, the solution was taken out for further catalytic experiments. The quantification of the conversion of $^{15}N_2$ into $^{15}NH_3$ was conducted by ^1H NMR spectroscopy.

The quantification of the ammonia yield rate in this work was conducted by the colorimetric indophenol blue method. The yield rate was calculated using the following equation:

$$\mathrm{Yield}_{\mathrm{NH_3}} = C_{\mathrm{NH_3}} \times \frac{V}{t} \times m_{\mathrm{cat.}},$$

where $C_{\mathrm{NH_3}}$ represents the concentration of ammonia, V represents the volume of the solution, t stands for the reaction time, and $m_{\mathrm{cat.}}$ is the mass of the catalyst. During the experiment, 1 ml of solution was centrifuged and transferred into a plastic bottle. This was followed by adding 1.25 ml of solution A, 150 μl of solution B, and 75 μl of solution C. The compositions of solutions A, B, and C are listed in Table S2 (SI). After the reaction time of 2 hours, the ammonia yield is determined by the absorption spectrum of UV-vis spectroscopy. By measuring the absorption peak intensity at $\lambda = 655$ nm, we can get the ammonia concentration in the solution by referring to the calibration curve and the equation (Fig. S4). The main byproduct of the nitrogen reduction reaction, N_2H_4, has also been detected by the colorimetric Watt and Chrisp method; the calibration curve is shown in Fig. S6.

4.5 Density functional theory simulation

First-principles calculations were performed utilizing the Vienna *Ab initio* Simulation Package (VASP) software employing the projector augmented wave (PAW) method. The Perdew–Burke–Ernzerhof (PBE) pseudopotential within the framework of the generalized gradient approximation (GGA) was employed. The van der Waals interactions between atoms were simulated by the DFT-D3 method. A 2 × 2 supercell with a ZnO (100) slab (six layers, bottom three fixed) and a 20 Å vacuum spacing was adopted; a 5 × 3 × 1 Γ-centered k-mesh was used for surface calculations. Long-range dispersion interactions were explicitly included using the Grimme DFT-D3 correction scheme without Becke–Johnson damping (D3, not D3BJ). A plane wave cutoff energy of 450 eV was utilized for the calculations. The calculation details are listed in the SI of S3.

Author contributions

J. X. W., H. Y. L., and J. M. W. conceived the idea for the project. J. X. W. and J. M. W. designed the experiments. J. X. W., H. Y. L., and Kuang Yuan Tu conducted the experiments and simulations. J. X. W., H. Y. L., and J. M. W. analyzed the experimental data and working principles, draw the figures, and prepared the manuscript.

Conflicts of interest

The authors declare that they have no known competing financial interests or personal relationships that could have appeared to influence the work reported in this paper.

Data availability

The datasets generated and/or analyzed during the current study are not publicly available due to proprietary restrictions, but are available from the corresponding author on reasonable request.

Supplementary information (SI) is available. See DOI: https://doi.org/10.1039/d5ta08002a.

Acknowledgements

The authors would like to thank the National Science and Technology Council, Taiwan (112-2224-E-007-004, 112-2221-E-007-085-MY3, 112-2218-E-006-021) and National Center for High-performance Computing for providing computational time and facilities, and for funding this research. This work was also financially supported by the "High Entropy Materials Center" from The Featured Areas Research Center Program within the framework of the Higher Education Sprout Project by the Ministry of Education (MOE).

References

1 S. Wang, F. Ichihara, H. Pang, H. Chen and J. Ye, *Adv. Funct. Mater.*, 2018, **28**, 1803309.
2 A. Klerke, C. H. Christensen, J. K. Nørskov and T. Vegge, *J. Mater. Chem.*, 2008, **18**, 2304–2310.
3 R. Lan, J. T. S. Irvine and S. Tao, *Int. J. Hydrogen Energy*, 2012, **37**, 1482–1494.

4 L. Wang, M. Xia, H. Wang, K. Huang, C. Qian, C. T. Maravelias and G. A. Ozin, *Joule*, 2018, **2**, 1055–1074.
5 M. J. Chalkley, M. W. Drover and J. C. Peters, *Chem. Rev.*, 2020, **120**, 5582–5636.
6 A. Fujishima and K. Honda, *Nature*, 1972, **238**, 37–38.
7 X. X. Guo, H. T. Du, F. L. Qu and J. H. Li, *J. Mater. Chem. A*, 2019, **7**, 3531–3543.
8 C.-G. Zhan, J. A. Nichols and D. A. Dixon, *J. Phys. Chem. A*, 2003, **107**, 4184–4195.
9 H.-P. Jia and E. A. Quadrelli, *Chem. Soc. Rev.*, 2014, **43**, 547–564.
10 X. Cui, C. Tang and Q. Zhang, *Adv. Energy Mater.*, 2018, **8**, 1800369.
11 X. Chen, N. Li, Z. Kong, W.-J. Ong and X. Zhao, *Mater. Horiz.*, 2018, **5**, 9–27.
12 Y. T. Lin, S. N. Lai and J. M. Wu, *Adv. Mater.*, 2020, **32**, 2002875.
13 A. Kumar and V. Krishnan, *Adv. Funct. Mater.*, 2021, **31**, 2009807.
14 C. Zhang, D. Qin, Y. Zhou, F. Qin, H. Wang, W. Wang, Y. Yang and G. Zeng, *Appl. Catal., B*, 2022, **303**, 120904.
15 F. He, B. Zhu, B. Cheng, J. Yu, W. Ho and W. Macyk, *Appl. Catal., B*, 2020, **272**, 119006.
16 J. M. Wu, W. E. Chang, Y. T. Chang and C. K. Chang, *Adv. Mater.*, 2016, **28**, 3718–3725.
17 M. B. Starr and X. Wang, *Sci. Rep.*, 2013, **3**, 2160.
18 J. M. Wu, Y. G. Sun, W. E. Chang and J. T. Lee, *Nano Energy*, 2018, **46**, 372–382.
19 C. Hu, F. Chen, Y. Wang, N. Tian, T. Ma, Y. Zhang and H. Huang, *Adv. Mater.*, 2021, **33**, 2101751.
20 J.-T. Lee, M.-C. Lin and J. M. Wu, *Nano Energy*, 2022, **98**, 107280.
21 W. Wu, L. Wang, Y. Li, F. Zhang, L. Lin, S. Niu, D. Chenet, X. Zhang, Y. Hao, T. F. Heinz, J. Hone and Z. L. Wang, *Nature*, 2014, **514**, 470–474.
22 K. T. Le, N. N. T. Pham, Y. S. Liao, A. Ranjan, H. Y. Lin, P. H. Chen, H. Nguyen, M. Y. Lu, S. G. Lee and J. M. Wu, *J. Mater. Chem. A*, 2023, **11**, 3481–3492.
23 Y.-J. Chung, C.-S. Yang, J.-T. Lee, G. H. Wu and J. M. Wu, *Adv. Energy Mater.*, 2020, **10**, 2002082.
24 S. Masimukku, Y.-C. Hu, Z.-H. Lin, S.-W. Chan, T.-M. Chou and J. M. Wu, *Nano Energy*, 2018, **46**, 338–346.
25 M. Chhowalla, H. S. Shin, G. Eda, L.-J. Li, K. P. Loh and H. Zhang, *Nat. Chem.*, 2013, **5**, 263–275.
26 D. Jariwala, V. K. Sangwan, L. J. Lauhon, T. J. Marks and M. C. Hersam, *ACS Nano*, 2014, **8**, 1102–1120.
27 S. Manzeli, D. Ovchinnikov, D. Pasquier, O. V. Yazyev and A. Kis, *Nat. Rev. Mater.*, 2017, **2**, 1–15.
28 H.-Y. Lin and J. M. Wu, *Adv. Energy Mater.*, 2024, 2402164.
29 H.-Y. Lin, K. T. Le, P.-H. Chen and J. M. Wu, *Appl. Catal., B*, 2022, **317**, 121717.
30 K. T. Le, N. N. T. Pham, Y.-S. Liao, A. Ranjan, H.-Y. Lin, P.-H. Chen, H. Nguyen, M. Y. Lu, S. G. Lee and J. M. Wu, *J. Mater. Chem. A*, 2023, **11**, 3481–3492.
31 P. H. Wu, H. Y. Lin, S. N. Lai, Y. C. Chen and J. M. Wu, *Nano Energy*, 2025, **144**, 111402.
32 Y.-C. Wang and J. M. Wu, *Adv. Funct. Mater.*, 2020, **30**, 1907619.
33 K. Y. Tu, H. Y. Lin, J. P. Chou and J. M. Wu, *Adv. Funct. Mater.*, 2025, 2424279, DOI: 10.1002/adfm.202424279.
34 Y. C. Chen, P. H. Chen, Y. S. Liao, J. P. Chou and J. M. Wu, *Small*, 2024, **20**, 2401116.
35 C.-Y. Tu and J. M. Wu, *Nano Energy*, 2021, **87**, 106131.
36 T.-M. Chou, S.-W. Chan, Y.-J. Lin, P.-K. Yang, C.-C. Liu, Y.-J. Lin, J.-M. Wu, J.-T. Lee and Z.-H. Lin, *Nano Energy*, 2019, **57**, 14–21.
37 Y. T. Wang, H.-Y. Lin, Y.-C. Chen, Y.-G. Lin and J. M. Wu, *Small Methods*, 2024, **8**, 2301287.
38 S. C. Chang, H. Y. Chen, P. H. Chen, J. T. Lee and J. M. Wu, *Appl. Catal. B Environ. Energy*, 2023, **324**, 122204.
39 M.-C. Lin, S.-N. Lai, K. T. Le and J. M. Wu, *Nano Energy*, 2022, **91**, 106640.
40 J. M. Wu, H. C. Shih and W. T. Wu, *J. Vac. Sci. Technol. B*, 2005, **23**, 2122–2126.
41 J. M. Wu and Y. R. Chen, *J. Phys. Chem. C*, 2011, **115**, 2235–2243.
42 J. A. Anta, E. Guillén and R. Tena-Zaera, *J. Phys. Chem. C*, 2012, **116**, 11413–11425.
43 A. Akyol, H. C. Yatmaz and M. Bayramoglu, *Appl. Catal., B*, 2004, **54**, 19–24.
44 K.-S. Hong, H. Xu, H. Konishi and X. Li, *J. Phys. Chem. Lett.*, 2010, **1**, 997–1002.
45 S. C. Chang, P. H. Chen, Y. C. Chen and J. M. Wu, *Int. J. Hydrogen Energy*, 2024, **50**, 15–25.
46 S. R. Jhang, H. Y. Lin, Y. S. Liao, J. P. Chou and J. M. Wu, *Nano Energy*, 2022, **102**, 107619.
47 C. Y. Tu and J. M. Wu, *Nano Energy*, 2021, **87**, 106131.
48 Y. Zhao, Y. Zhao, R. Shi, B. Wang, G. I. N. Waterhouse, L.-Z. Wu, C.-H. Tung and T. Zhang, *Adv. Mater.*, 2019, **31**, 1806482.
49 H. Hirakawa, M. Hashimoto, Y. Shiraishi and T. Hirai, *J. Am. Chem. Soc.*, 2017, **139**, 10929–10936.
50 J. M. Wu, C. W. Fang, L. T. Lee, H. H. Yeh, Y. H. Lin, P. H. Yeh, L. N. Tsai and L. J. Lin, *J. Electrochem. Soc.*, 2011, **158**, K6–K10.
51 D. Chen, Z. Wang, T. Ren, H. Ding, W. Yao, R. Zong and Y. Zhu, *J. Phys. Chem. C*, 2014, **118**, 15300–15307.
52 X. Xiong, Y. Wang, J. Ma, Y. He, J. Huang, Y. Feng, C. Ban, L.-Y. Gan and X. Zhou, *Appl. Surf. Sci.*, 2023, **616**, 156556.
53 Y. Xu, H. Li, B. Sun, P. Qiao, L. Ren, G. Tian, B. Jiang, K. Pan and W. Zhou, *Chem. Eng. J.*, 2020, **379**, 122295.
54 X. Zhang, J. Qin, Y. Xue, P. Yu, B. Zhang, L. Wang and R. Liu, *Sci. Rep.*, 2014, **4**, 4596.
55 W. Tu, Y. Xu, J. Wang, B. Zhang, T. Zhou, S. Yin, S. Wu, C. Li, Y. Huang, Y. Zhou, Z. Zou, J. Robertson, M. Kraft and R. Xu, *ACS Sustain. Chem. Eng.*, 2017, **5**, 7260–7268.
56 C. Fu, M. Zhao, X. Chen, G. Sun, C. Wang and Q. Song, *Appl. Catal., B*, 2023, **332**, 122752.
57 K. S. Gerace, J. C. Mauro and C. A. Randall, *J. Am. Ceram. Soc.*, 2021, **104**, 1915–1944.
58 A. A. Issa, M. A. Al-Maadeed, A. S. Luyt, D. Ponnamma and M. K. Hassan, *C*, 2017, **3**, 30.

59 J. Yuan, W. Feng, Y. Zhang, J. Xiao, X. Zhang, Y. Wu, W. Ni, H. Huang and W. Dai, *Adv. Mater.*, 2024, **36**, 2303845.
60 M. A. Mushtaq, M. Arif, X. Fang, G. Yasin, W. Ye, M. Basharat, B. Zhou, S. Yang, S. Ji and D. Yan, *J. Mater. Chem. A*, 2021, **9**, 2742–2753.
61 S. Ghoshal, A. Ghosh, P. Roy, B. Ball, A. Pramanik and P. Sarkar, *ACS Catal.*, 2022, **12**, 15541–15575.
62 G. Henkelman, A. Arnaldsson and H. Jónsson, *Comput. Mater. Sci.*, 2006, **36**, 354–360.
63 E. Sanville, S. D. Kenny, R. Smith and G. Henkelman, *J. Comput. Chem.*, 2007, **28**, 899–908.
64 W. Tang, E. Sanville and G. Henkelman, *J. Phys.: Condens. Matter*, 2009, **21**, 084204.
65 M. Yu and D. R. Trinkle, *J. Chem. Phys.*, 2011, **134**, 6.
66 X. Ma, Y. Lv, J. Xu, Y. Liu, R. Zhang and Y. Zhu, *J. Phys. Chem. C*, 2012, **116**, 23485–23493.
67 K. S. Hong, H. F. Xu, H. Konishi and X. C. Li, *J. Phys. Chem. Lett.*, 2010, **1**, 997–1002.
68 Y. C. Chen, Y. S. Liao, P. H. Chen, J. P. Chou, C. K. Tsai, Y. D. Lin, Y. G. Lin, Y. R. Peng and J. M. Wu, *ACS Nano*, 2025, **19**, 36602–36613.
69 K. Y. Tu, H. Y. Lin, J. P. Chou and J. M. Wu, *Adv. Funct. Mater.*, 2025, **35**, 2424279.
70 Y. Wan, J. Xu and R. Lv, *Mater. Today*, 2019, **27**, 69–90.
71 W. Peng, M. Luo, X. Xu, K. Jiang, M. Peng, D. Chen, T.-S. Chan and Y. Tan, *Adv. Energy Mater.*, 2020, **10**, 2001364.
72 S. Yuan, H. Ren, G. Meng, W. Zhao, H. Zhu and W. Guo, *Appl. Surf. Sci.*, 2021, **555**, 149682.